5 Simulation of global warming

5.1 Temperature

Figure 21 shows the time evolution of the area-averaged, annual-mean surface air temperature for the C and G runs. There remains a weak secular trend in the Southern Hemisphere in the C run, which is, however, smaller than the CO_2 warming signal. The globally averaged surface air temperature difference, G-C, increases by 1.6 °C over the seventy-year period.

Murphy (1992) and Cubasch *et al.* (1992) have mentioned initial slow rise in the globally averaged surface air temperature in relation to the initial spin-up problem or the cold start problem (Hasselmann *et al.*, 1992). However, in our experiment, the globally averaged surface air temperature increased almost linearly (see Fig. 21).

The latitude-time section of zonally averaged surface air temperature change (Fig. 22) shows that this delay of the temperature increase in the Southern Hemisphere, particularly around 50°S, is dominant, as already pointed out by Stouffer *et al.* (1989). It is also noteworthy that the surface air temperature increase in the Arctic region is rather small until year 50. Thereafter it increases at a higher rate. This has not been stressed before, although a similar tendency is seen in Fig.1 of Stouffer *et al.* (1989) and Fig.1f of Meehl *et al.* (1993).

5.2 EOF analysis

The first EOF of the SST of the G run is almost identical to that of the first mode of the EOF analysis for the annual mean SST difference (Fig. 23). The coefficient showed an overall linear increasing trend over 70 years, indicating that this is a response mode to the gradual increase in CO_2. A large SST rise was found for the Sea of Okhotsk. A related mechanism is presented in the next subsection. Between 40°S and 60°S, where most of the surface is covered by ocean, the SST rise is generally delayed, as in other studies (Stouffer *et al.*, 1989; Murphy, 1992; Cubasch *et al.*, 1992; Meehl et al, 1993). There is dominant warming in the North Pacific, the North Atlantic and the subtropical latitudes of the Southern Hemisphere. The warming in the North Atlantic may reflect the fact that the meridional circulation in the North Atlantic is weak in the present experiment.

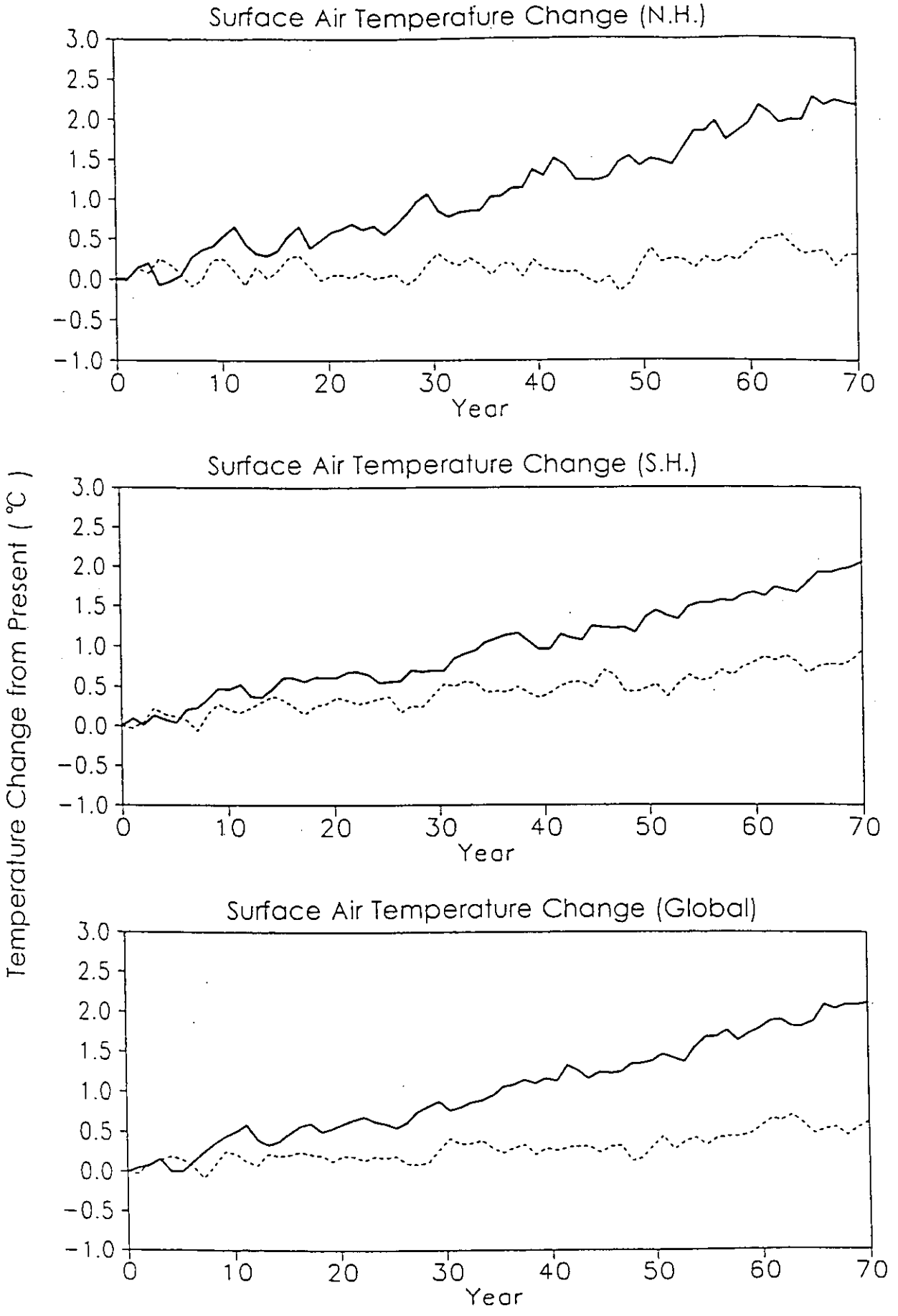

Fig. 21 Time evolution of annual-mean surface air temperature change averaged over the Northern Hemisphere (top), the Southern Hemisphere (middle) and the globe (bottom). Solid and dashed lines indicate the G run and the C run, respectively. The zero point is the annual mean for the first year of the C run. In the G run, CO_2 concentration is increased at a compound annual rate of 1%, while it remains fixed in the C run.

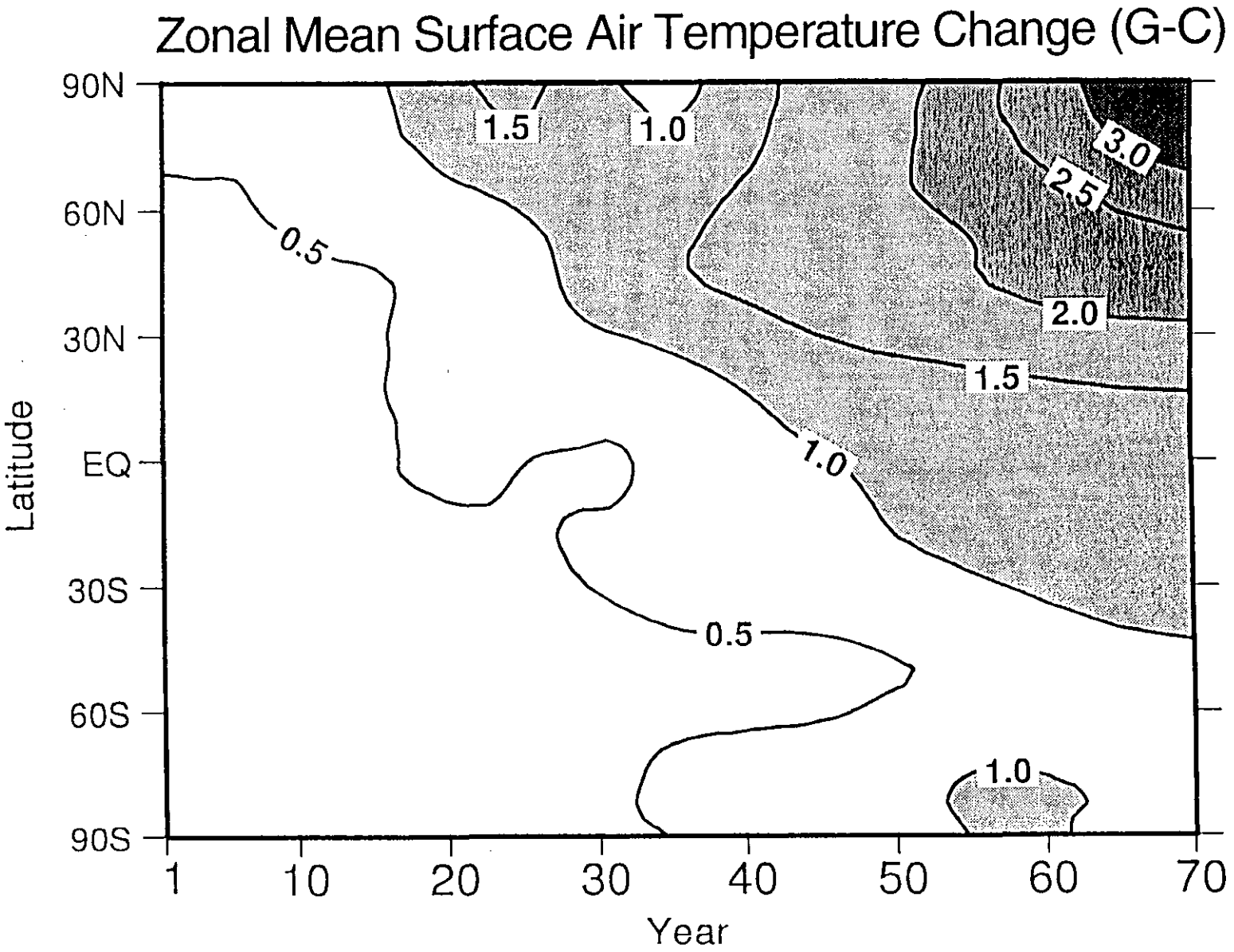

Fig. 22 Latitude-time section of zonally averaged surface air temperature difference, which is taken between the G run and the C run at the same time instance. Periods shorter than 12 years have been filtered out.

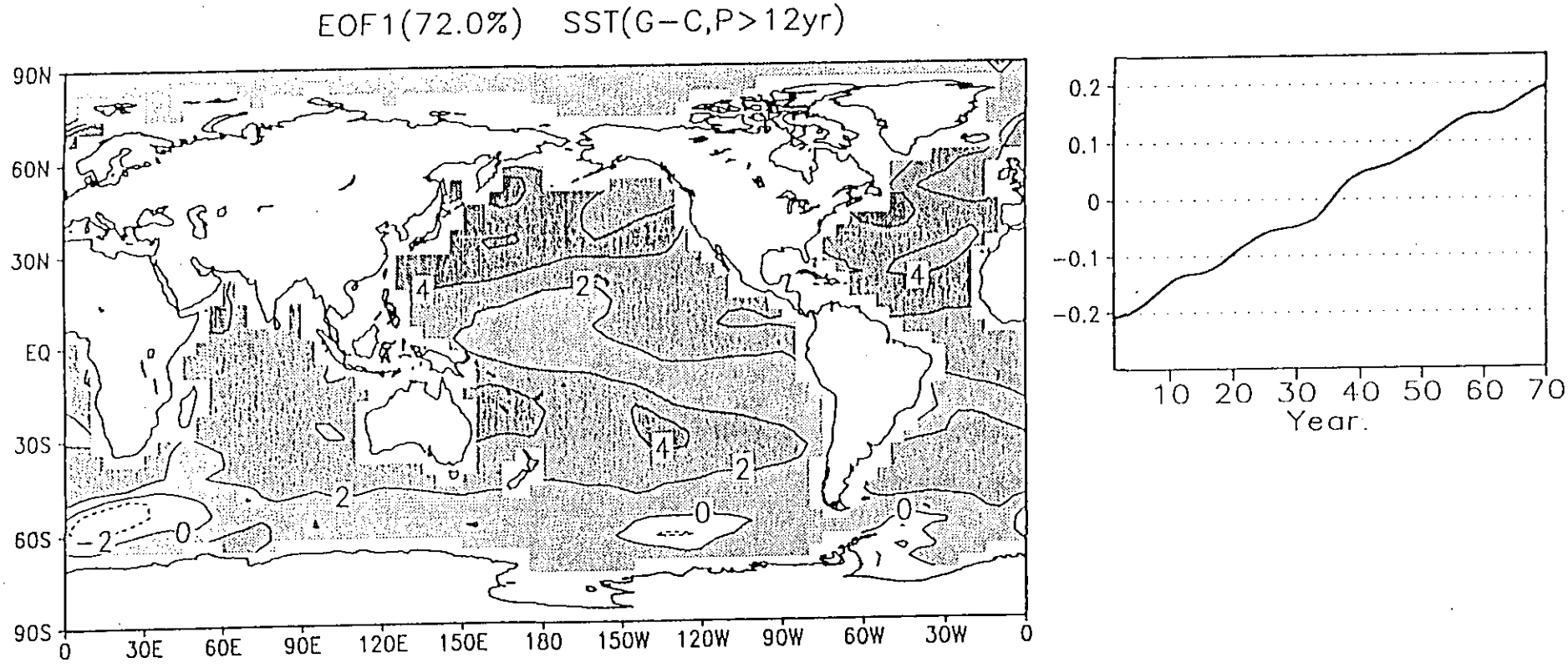

Fig. 23 The first mode of the empirical orthogonal function (EOF) analysis of the annually averaged SST difference between the G run and the C run. (left) Spatial pattern, (right) time evolution of the amplitude of the mode. Periods shorter than 12 years have been filtered out. The contribution of this mode to total variability is shown in the parentheses at the top of the figure.

As expected, the spatial pattern of the increase in annual mean surface air temperature during 70 years estimated from a linear regression of the temperature difference G - C (Fig. 24) is almost identical to that over the ocean (Fig. 23). There are pronounced increases in temperature over the continents at mid-latitudes in both hemispheres. This contrast between the land and sea warming was explained by Saito and Tokioka (1994). The most prominent increase was found over the sea of Okhotsk.

The fact that the second EOF of SST for the G run (Fig. 25) had a spatial pattern almost identical to that for the first EOF for the C run (see Fig. 19) indicates that this is an internal mode of the climate system. A similar correspondence between the first EOF for the control run and the second EOF for the transient CO_2 run can be seen in Fig.12 of Cubasch *et al.* (1992), although the spatial pattern of the mode is different from that found in the present experiment.

It can be seen that the coefficient of the second EOF for the G run also shows dominant 6-year cycles, and interdecadal modulations of these cycles of about 30 years. Another important point to be noted is that the interdecadal time evolutions of both modes are almost identical until the year 30 or so. This type of variation could be little affected by increases in CO_2 concentration, and thus could be predicted about 30 years ahead. The mechanisms of the variability of this mode are being studied and will be reported separately. This mode has a characteristic structure in the Pacific sub-tropical gyre down to about 500 m depth, which is the main reason for the long time predictability of over 30 years.

A quick comparison of the variability in the El Niño time scale between the time evolutions presented in Figs. 19 and 25 does not show clear differences. Here, we do not make any conclusive statements about changes in El Niño phenomena due to increases in CO_2. This point will be studied further by extending the time integration period of the G run.

5.3 Sea ice

Interdecadal as well as interannual variations are apparent in the simulated sea ice volume for the Northern Hemisphere for the C and G runs (Fig. 26). The interdecadal variations have amplitudes comparable to those due to the doubled CO_2 radiative forcing around the year 70, indicating that

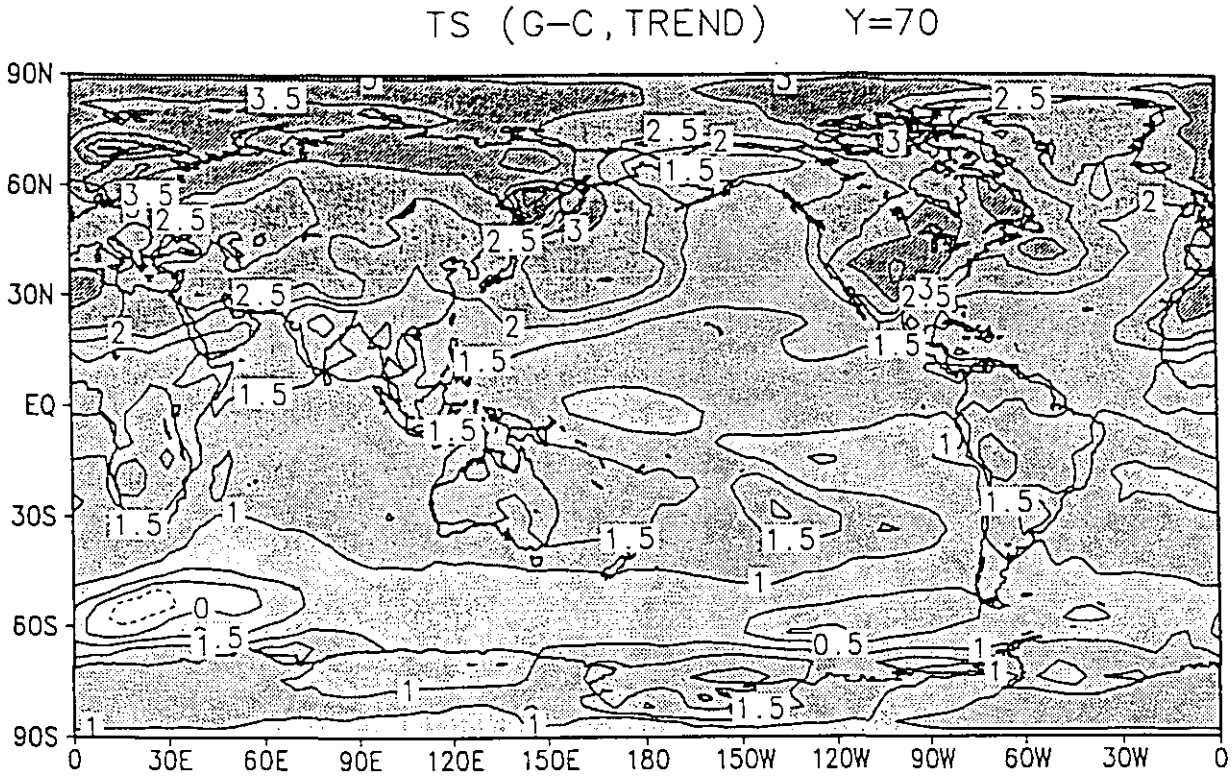

Fig. 24 The increase in surface air temperature after 70 years estimated from a linear regression of the temperature difference, G-C.

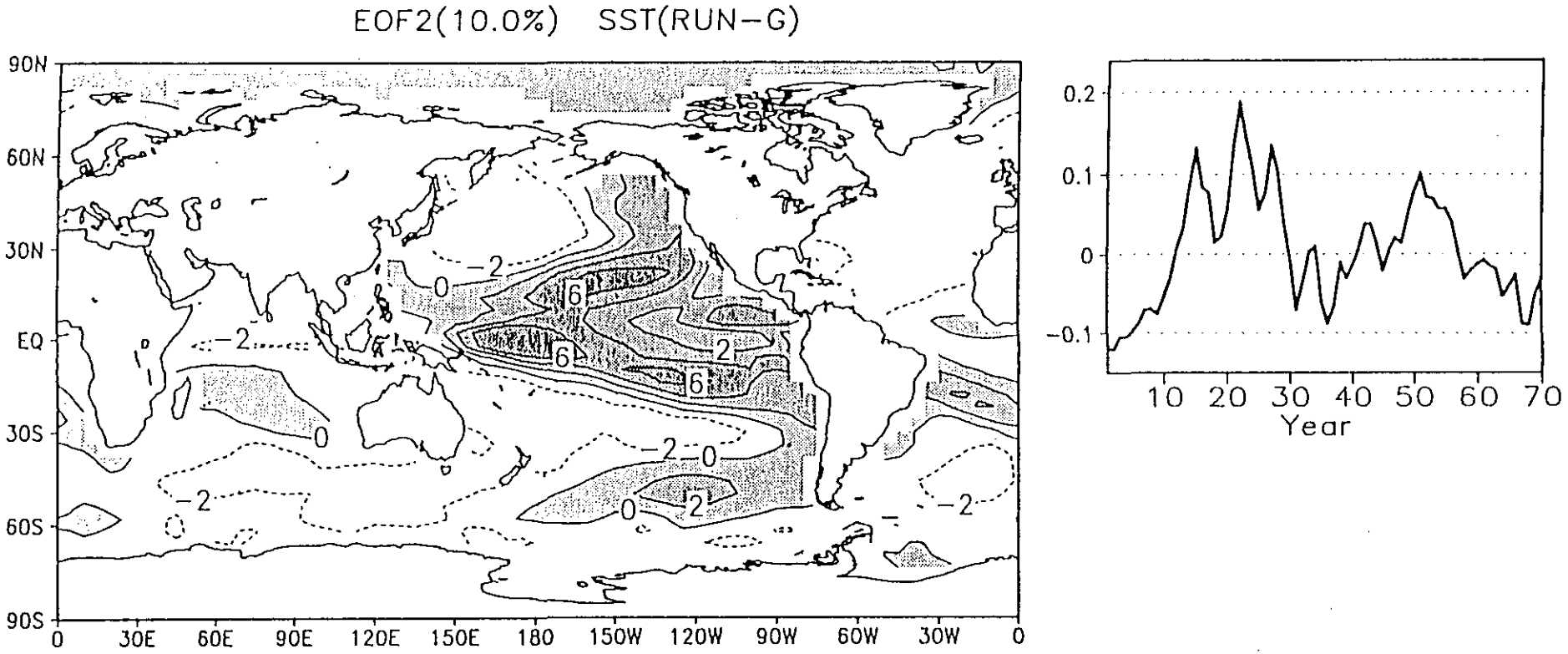

Fig. 25 The second mode of the EOF analysis of the annually averaged SST for the G run. No low-pass filter has been applied.

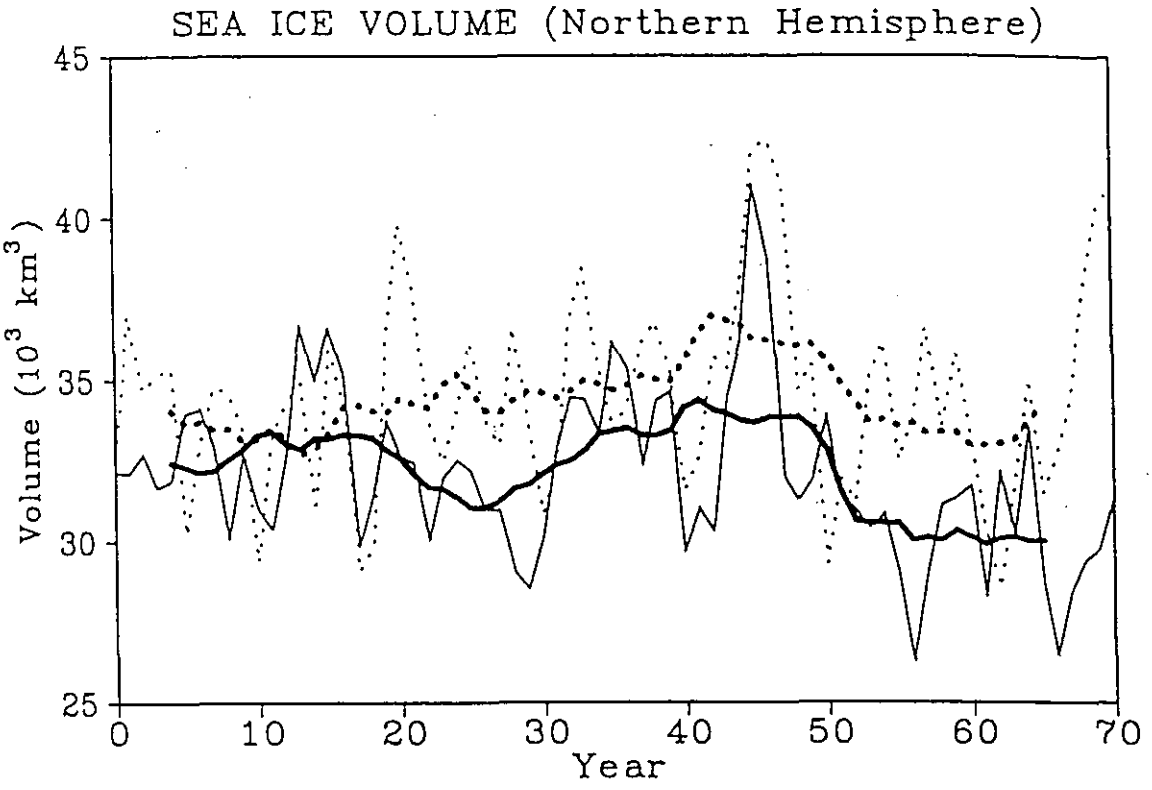

Fig. 26 Temporal variation of sea ice volume ($10^3 km^3$) in the Northern Hemisphere for the G run (solid lines) and the C run (dotted lines). Thin and thick lines indicate annual means and 11-year running means, respectively.

the temporal evolution of CO_2 warming in the northern high latitudes is much affected by not only the amplitude but also the phase of the natural variability in sea ice. In the present experiment, a transition from a positive to negative anomaly phase in sea ice volume occurs around year 50, so that a delay of the warming is found before that time and an acceleration afterwards. This ice variability may be indicative of some kind of global low-frequency variability that is most readily manifested in the sea ice characteristics.

Although the temperature increase occurs predominantly at high latitudes of the Northern Hemisphere, it is not as large as that from the GFDL result (Stouffer *et al.*, 1989). Since no leads were considered in the GFDL sea ice model, a different feedback mechanism related to leads may be operating in the present experiment over the region covered with sea ice.

The variation of the surface air temperature at the north pole during the C run was positively correlated with that of upward energy flux, suggesting that the surface air temperature is much affected by local heating in the polar region (Fig. 27).

The increase in water vapor at low levels due to the evaporation over leads increases cloudiness, helping to suppress the SST increase in summer by preventing solar fluxes from heating the surface (see Fig. 27). However, clouds have a greenhouse effect for longwave radiation fluxes so that the net radiative energy fluxes act as a positive feedback on SST rise. On the other hand, the sensible and latent heat fluxes from leads increase in proportion to the increase in lead area when SST increases. This works as a negative feedback. Another negative feedback in sea ice regions is due to increase in heat conduction as ice thickness decreases. However, the feedback in lead regions is much stronger than that in sea ice regions. As a result, the negative feedback effects of sensible and latent heat fluxes dominate SST change. However, only negative feedback due to heat conduction operates in the sea ice models with no leads. Thus, the difference in the magnitude of the negative feedback may be responsible for the smaller temperature rise in the Arctic in the present simulation than that in the GFDL's simulation.

An early and large increase in temperature occurred over the Okhotsk Sea in the G run. It may be inferred that the sea ice feedback effect is responsible for the warming over there because the Okhotsk Sea locates the southernmost boundary of sea ice formation in the Northern Hemisphere.

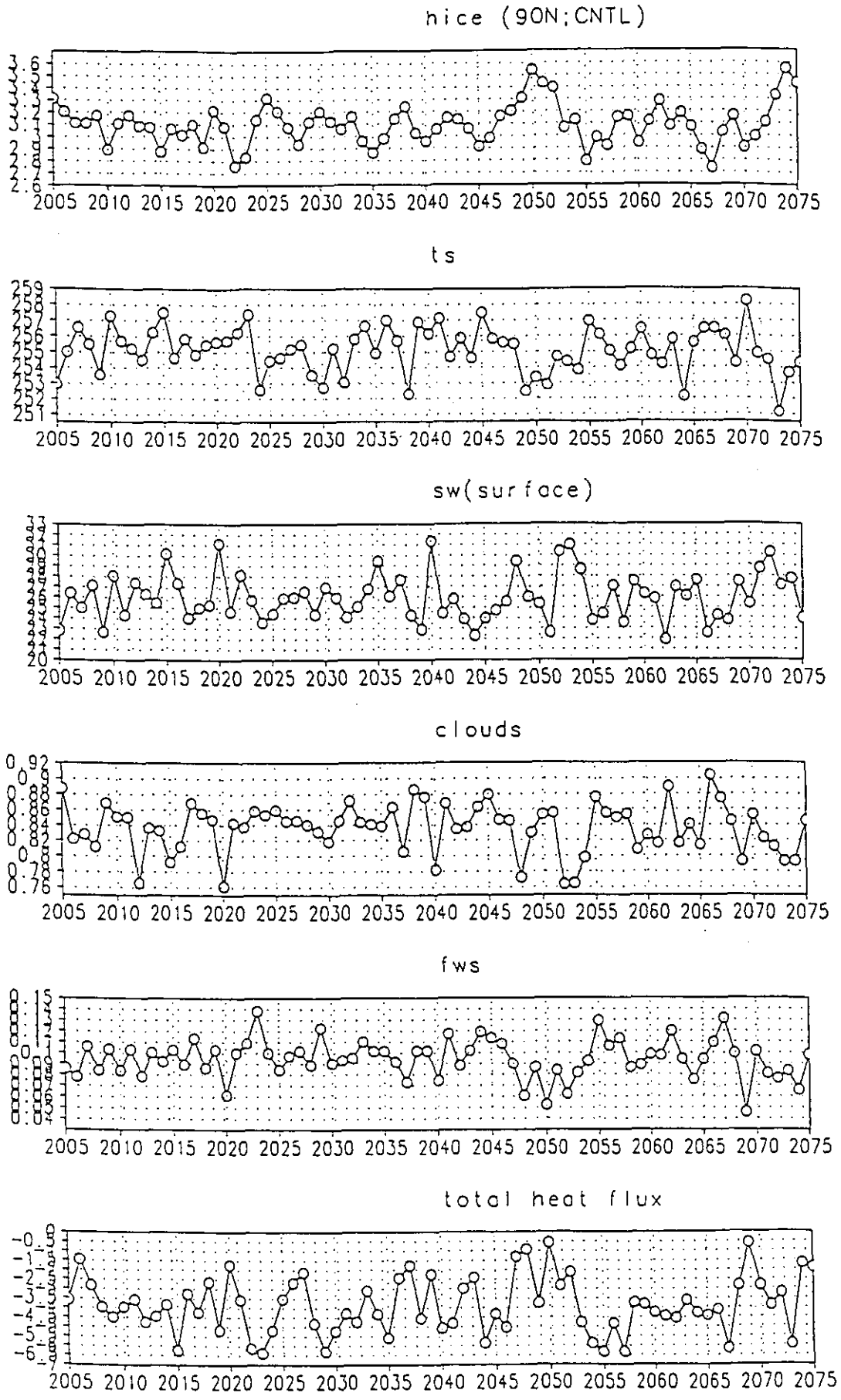

Fig. 27 Temporal annual mean variations of, from top to bottom, thickness of sea ice (m), surface air temperature (K), downward shortwave flux at the surface (W/m^2), cloudiness, evaporation (upward latent energy flux) (mm/day; $29.1 W/m^2$) and downward total energy flux at the surface (W/m^2) for the C run at the north pole.

Indeed, the surface air temperature increased rapidly after the sea ice receded (Fig. 28). However, the upward total heat flux subsequently decreased, contrary to the response expected from the sea ice feedback in polar regions described above.

No systematic trends in precipitation and evaporation can be seen (see Fig. 28), so the change in sea ice formation cannot be due to change in SSS. Therefore, the temporal change in the physical quantities (see Fig. 28) suggests that the warming is not caused by local thermal forcing by sea ice.

Wave-number 3 patterns are clearly seen in the change (G - C) in both the 500 hPa geopotential height and surface air temperature fields (Fig. 29), although the phase is shifted westward for the latter. By assuming geostrophic flows, the Okhotsk Sea and other regions of substantial warming correspond to increases in southerly winds, i.e., warm air advection. These observations suggest that the warming is much affected by a stationary wave which may be induced by a shift of the subtropical jet.

5.4 Two-dimensional mean fields

In the following discussion, comparisons will be made between mean fields for the C and G runs averaged over the same period, years 51 to 70. A large cooling was found in the stratosphere (Fig. 30), as expected from the heat balance. However, since the cooling was larger at higher latitudes, polar night jets were intensified (Fig. 31).

The water vapor content of the atmosphere increased due to warming in the troposphere (Figs. 30 and 32). However, the relative humidity decreased in the troposphere except for the upper troposphere and at high latitudes (Fig. 33). This pattern of the change resembles that for clouds (Fig. 34) because the present cloud model depends basically on relative humidity. A similar response was discussed in detail by Manabe and Wetherald (1988).

An effect of enhanced cumulus convection can be seen in the difference field of total heating (Fig. 35) and its components (Figs. 36-40). The enhanced tropical peak around 300 hPa for cumulus heating (Fig. 38) corresponds to that for relative humidity (Fig. 33) and clouds (Fig. 34), which is consistent with the enhancement of solar absorption (Fig. 36) and longwave cooling (Fig. 37).

A notable decrease in meridional eddy transport of momentum (Fig. 41) and heat (Fig. 42)

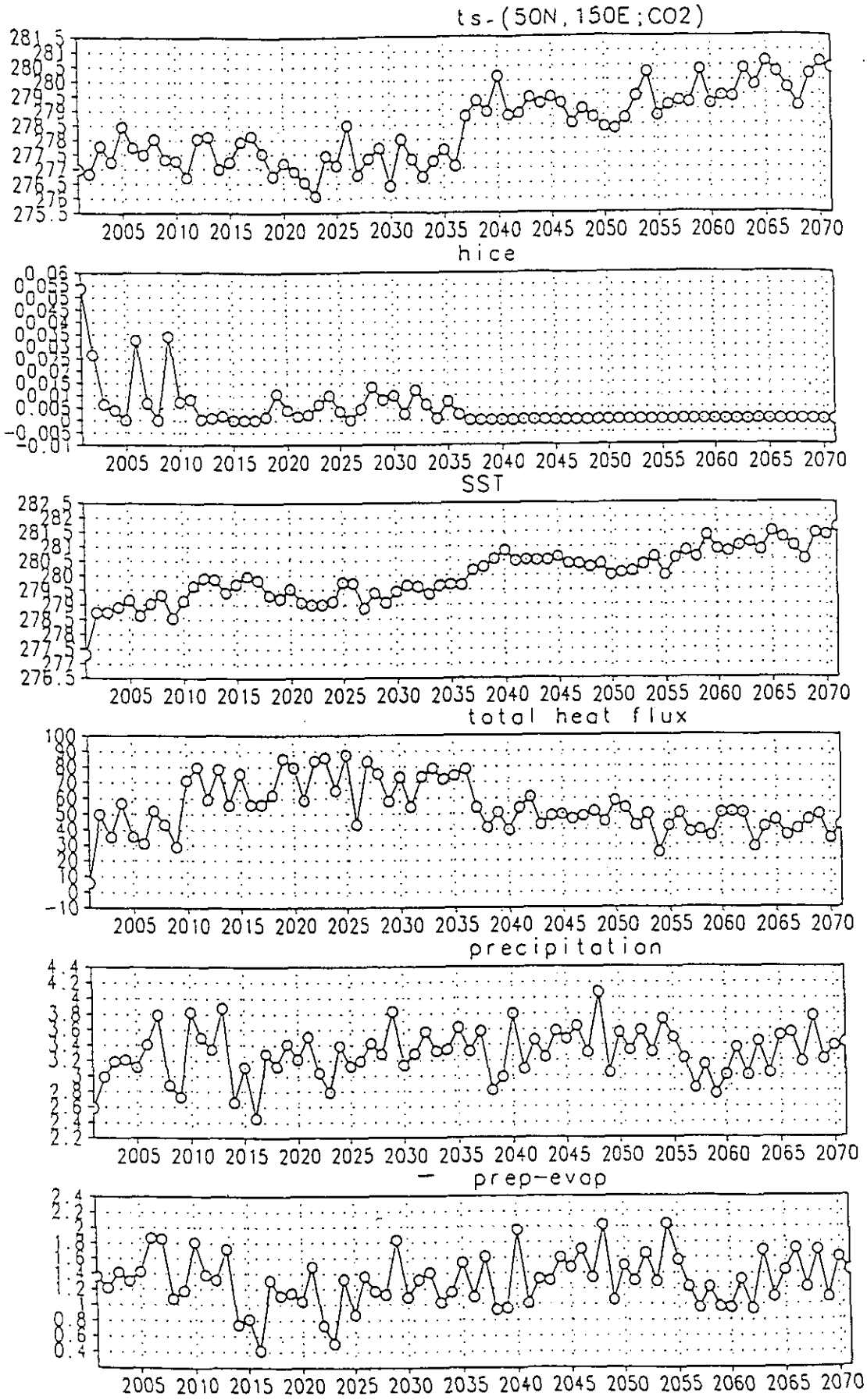

Fig. 28 Temporal annual mean variations of, from top to bottom, surface air temperature (K), thickness of sea ice (m), sea surface temperature (K), upward total energy flux at the surface (W/m^2), precipitation (mm/day), and precipitation - evaporation (mm/day) for the C run at a grid point (50°N, 150°E) in the Okhotsk Sea.

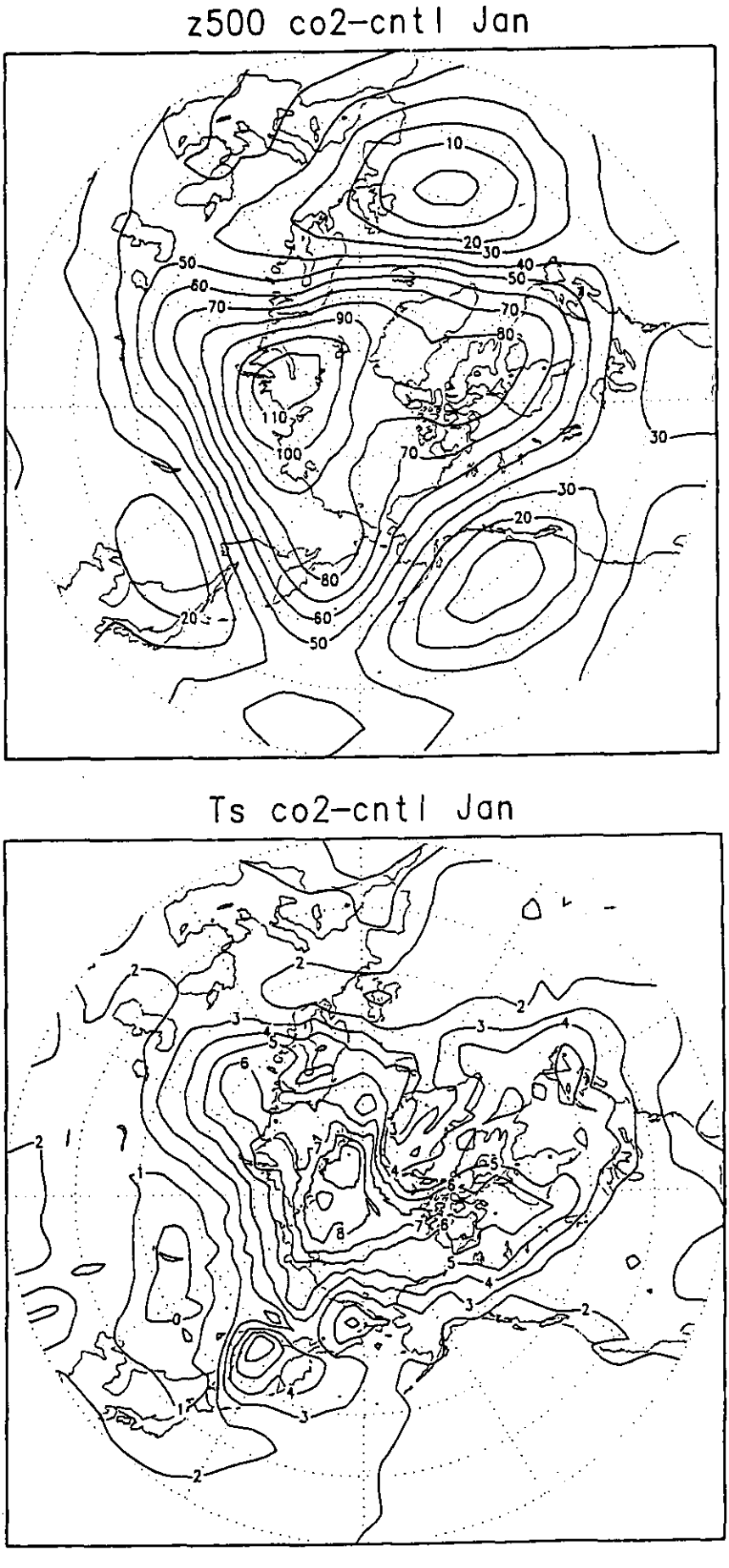

Fig. 29 Change in decadally-averaged (years 61-70) monthly-mean differences between the G and C runs for geopotential height (m) (upper panel) and surface air temperature (K) (lower panel) at 500 hPa in January.

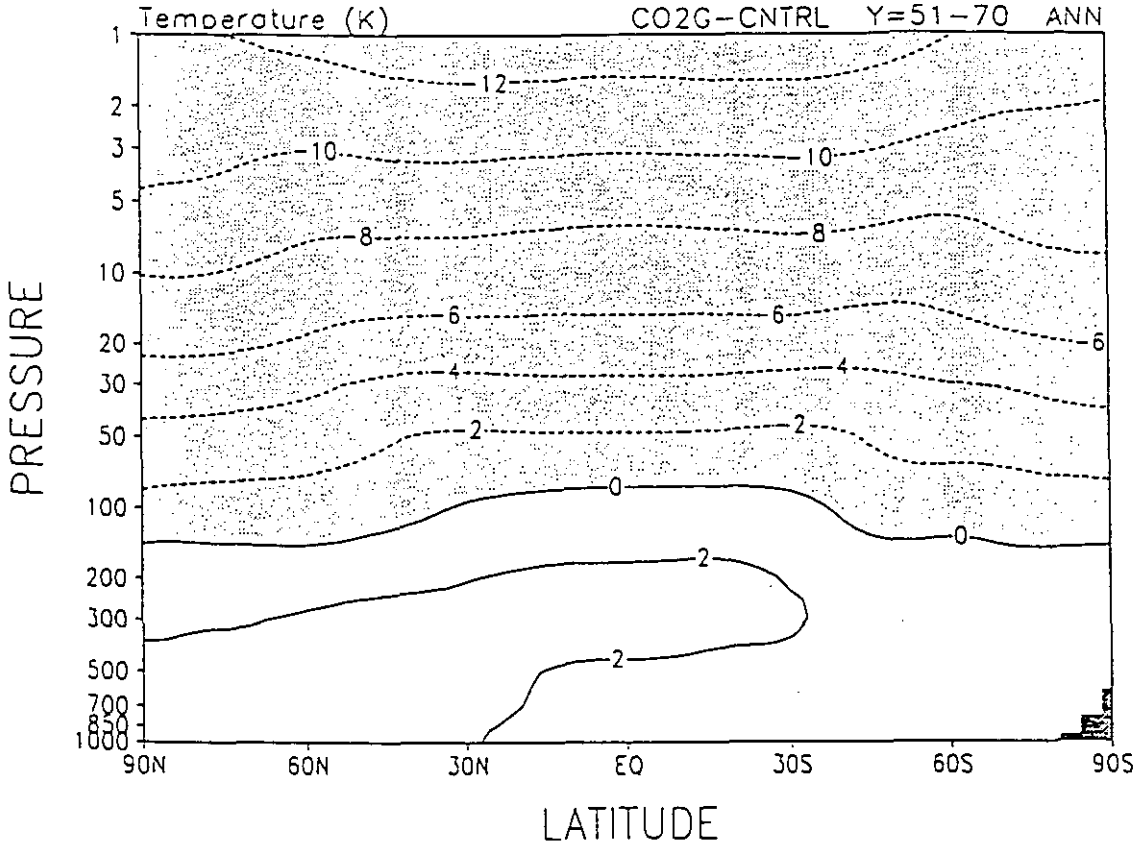

Fig. 30 Change, G - C, in the latitude-height cross section of zonally-averaged annual-mean temperature (mean of years 51-70). Contour interval is 2 °C.

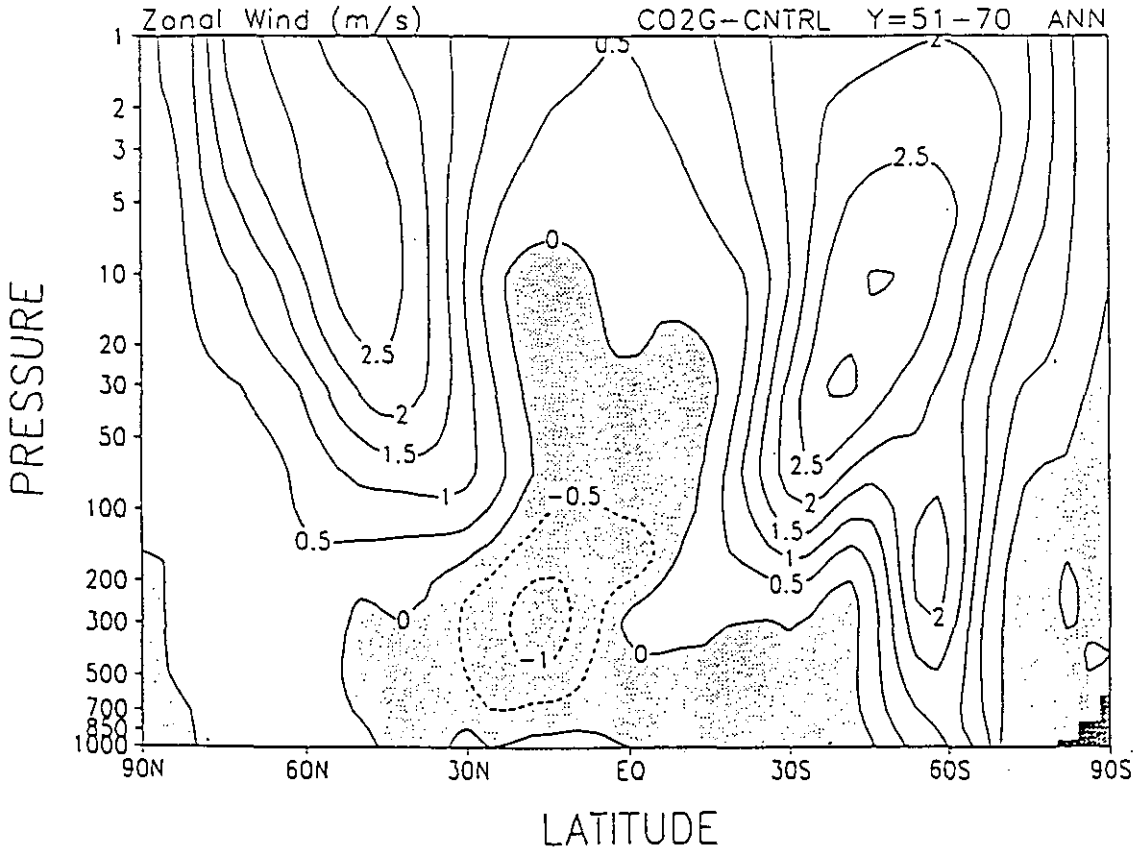

Fig. 31 As in Fig. 30 but for zonal wind. Contour interval is 0.5 m/s.

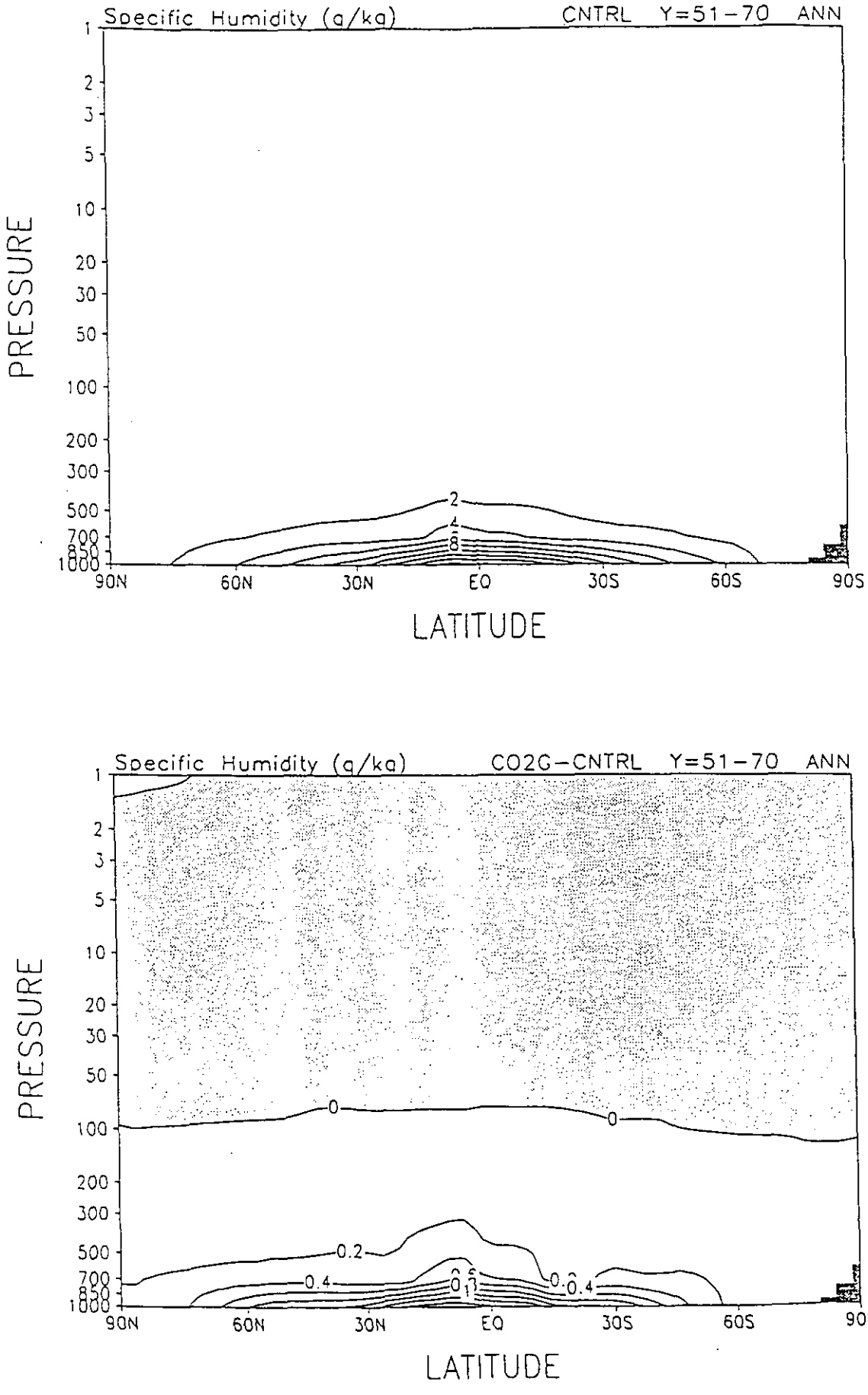

Fig. 32 Latitude-height cross section of zonally-averaged annual-mean specific humidity for the C run (upper panel) and its change, G - C, (lower panel). Both are averaged over years 51-70. Contour intervals are 2 g/kg (upper panel) and 0.2 g/kg (lower panel).

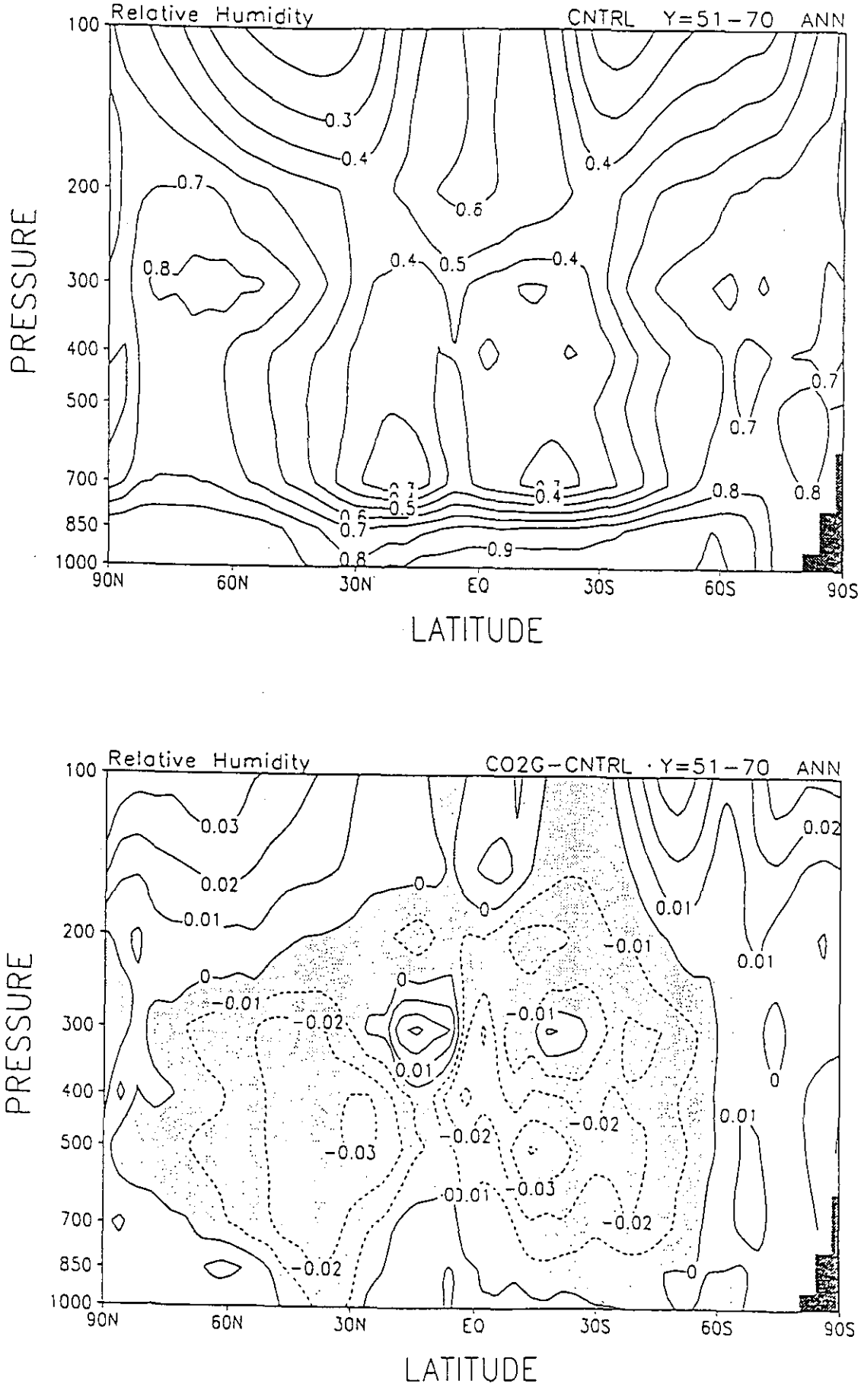

Fig. 33 As in Fig. 32 but for relative humidity. Contour intervals are 10 % (upper panel) and 1 % (lower panel).

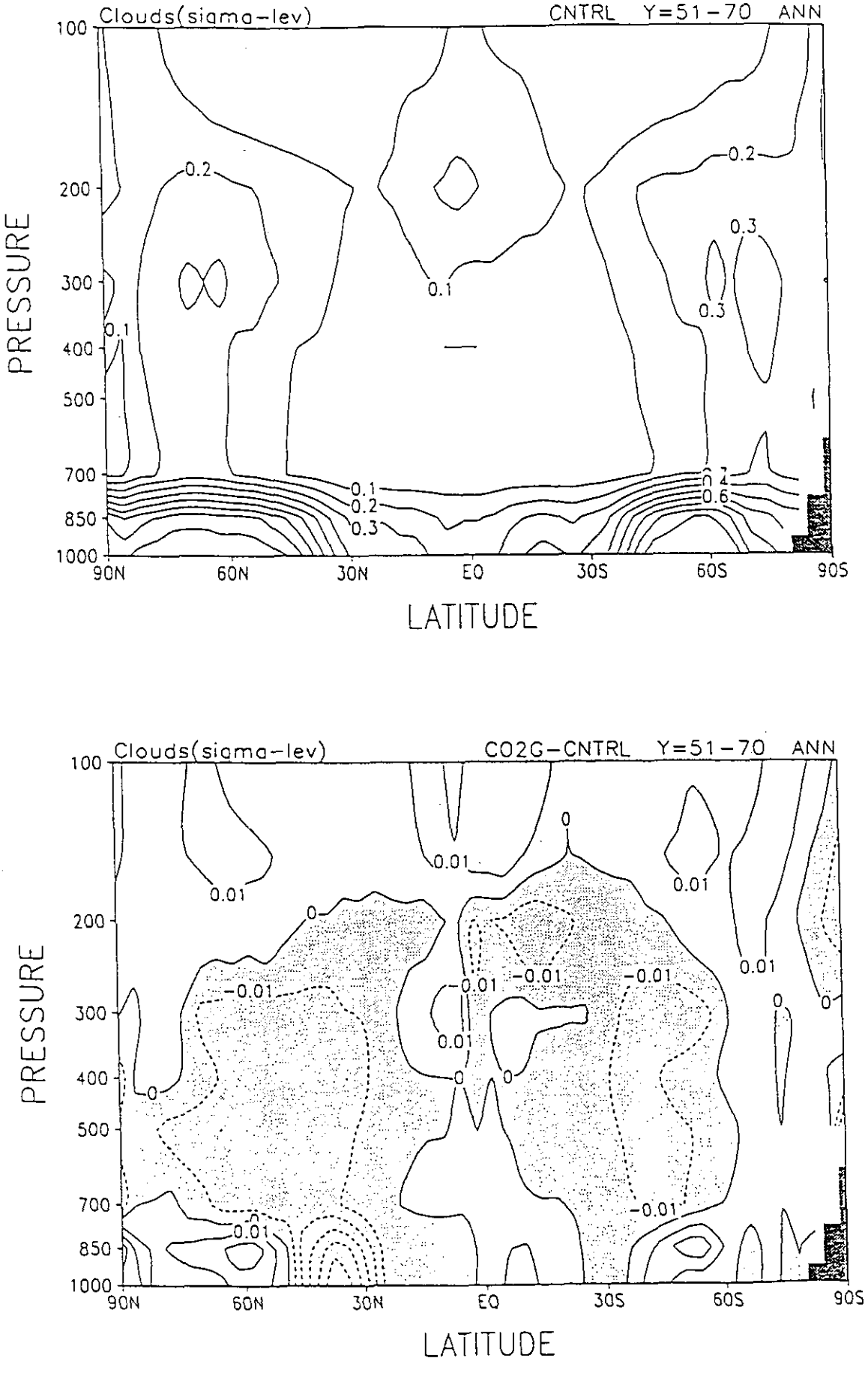

Fig. 34 As in Fig. 32 but for cloud amount. Contour intervals are 10 % (upper panel) and 1 % (lower panel).

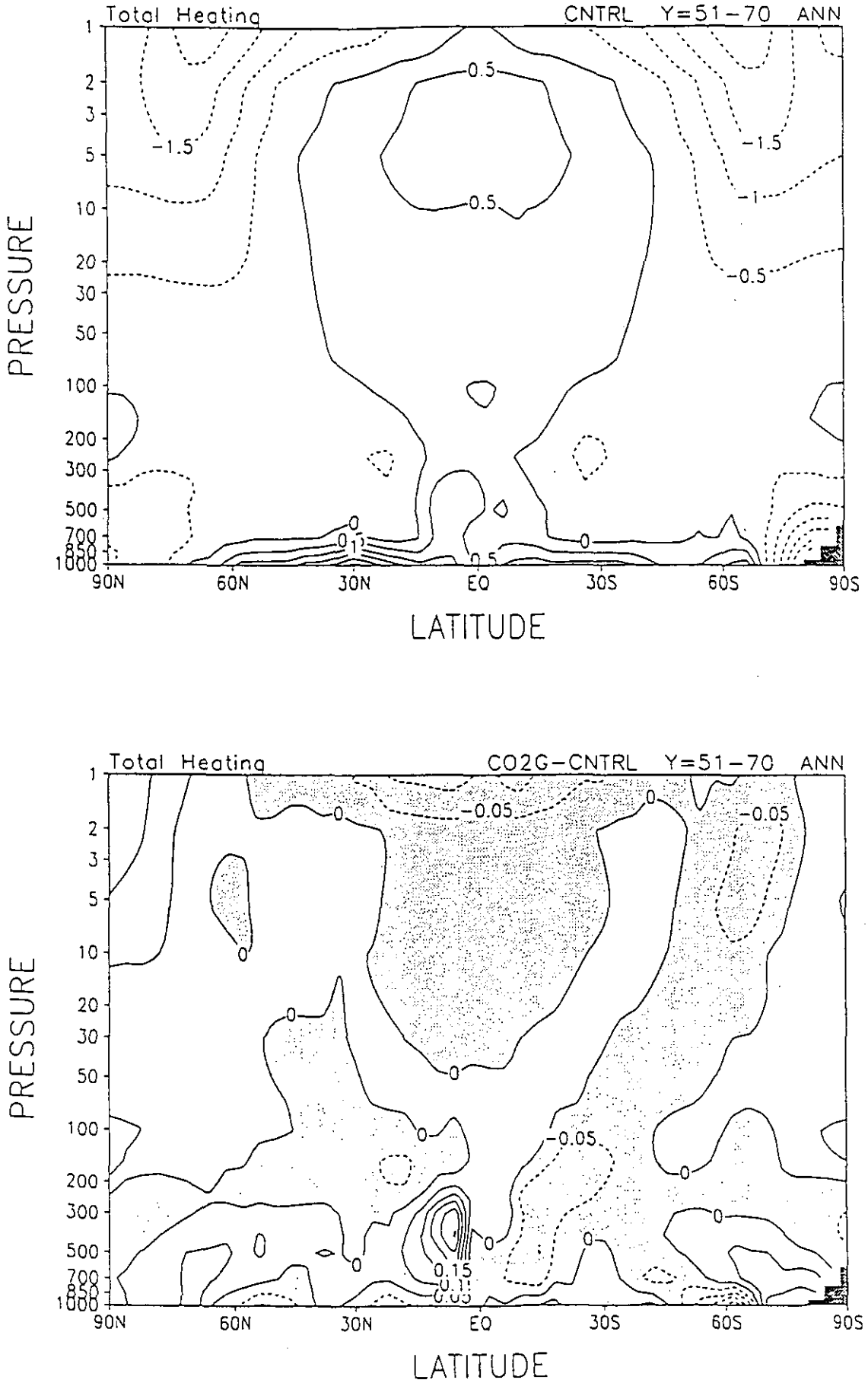

Fig. 35 As in Fig. 32 but for total diabatic heating. Contour intervals are 0.5 K/day (upper panel) and 0.05 K/day (lower panel).

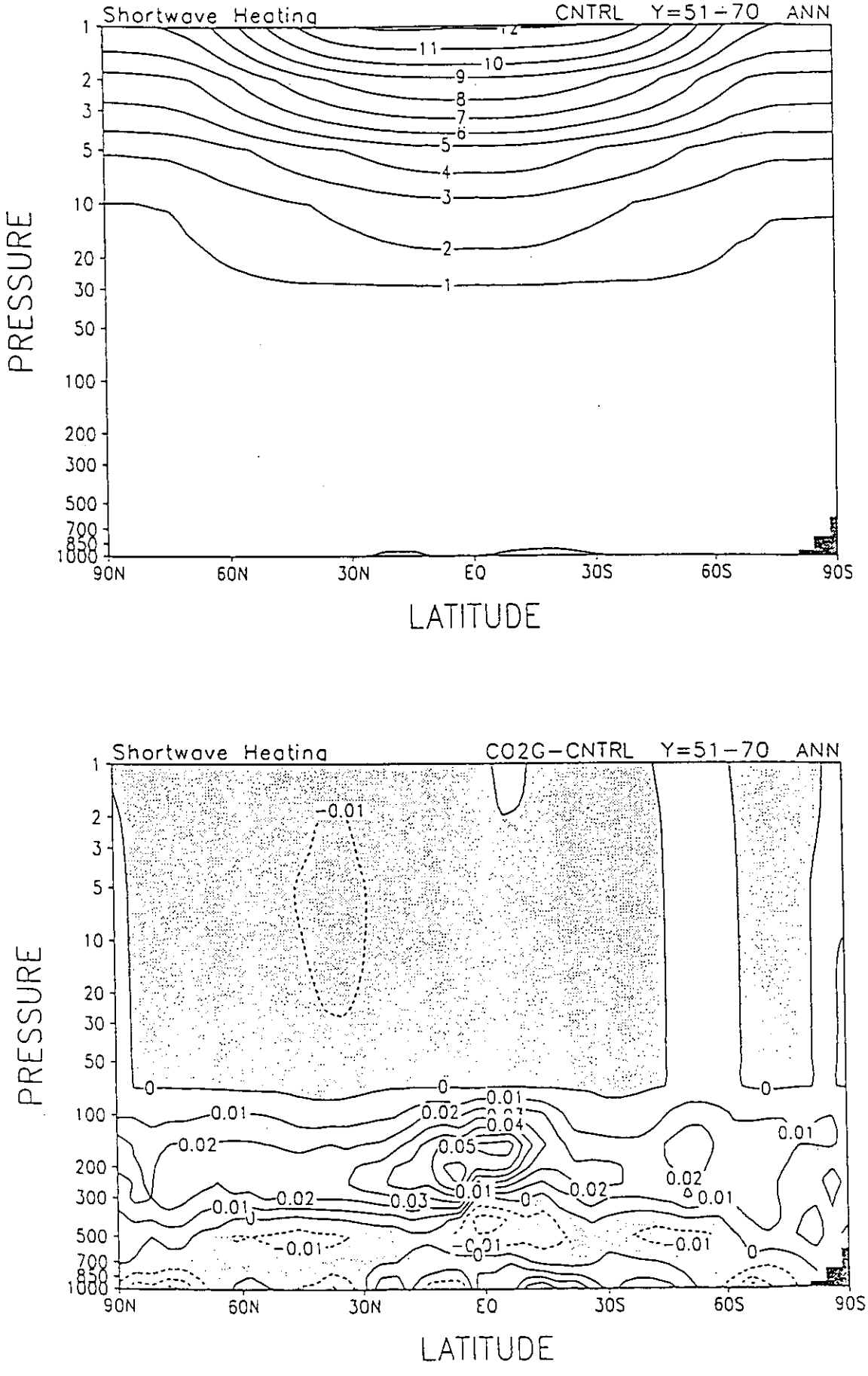

Fig. 36 As in Fig. 32 but for shortwave heating. Contour intervals are 1 K/day (upper panel) and 0.01 K/day (lower panel).

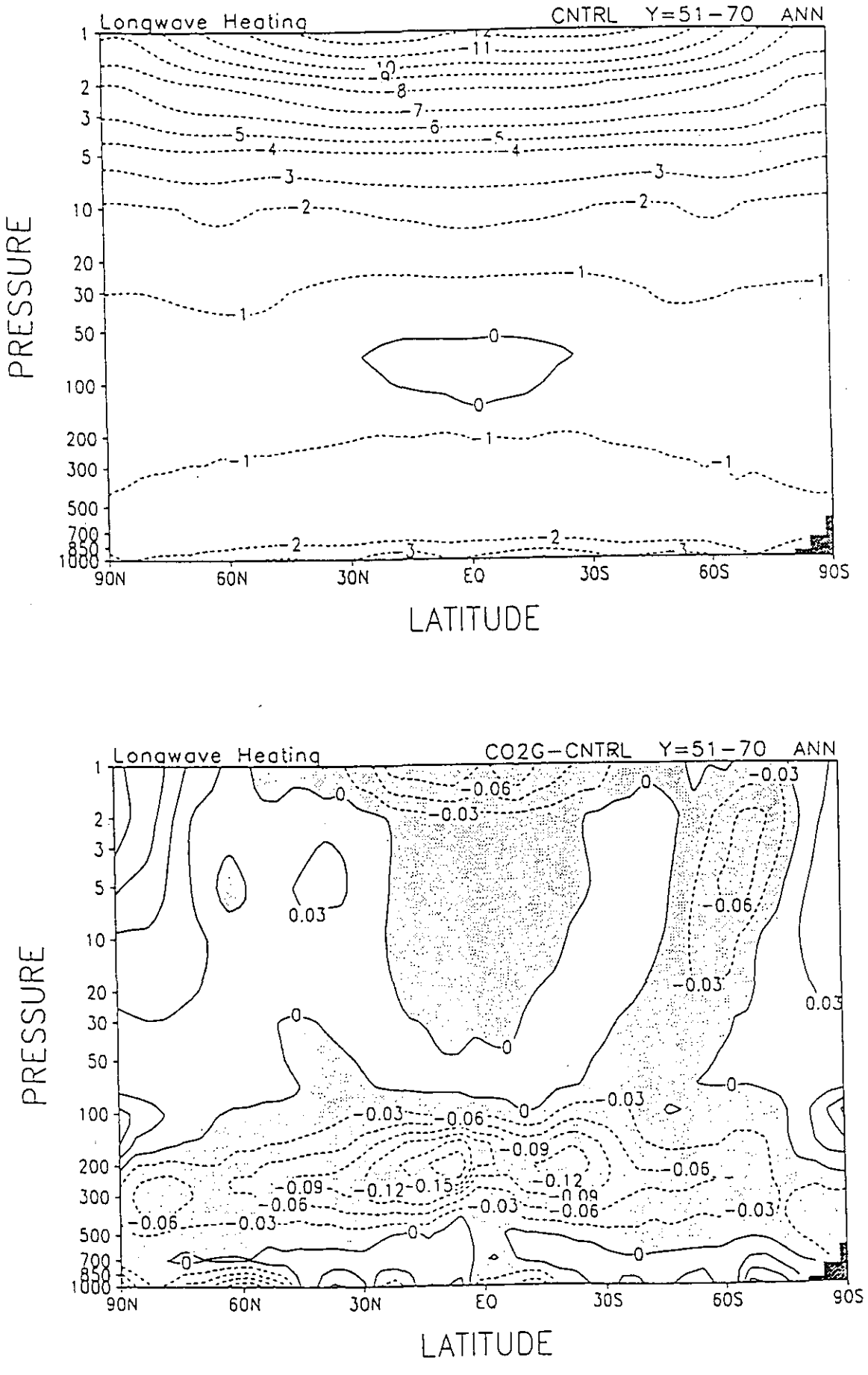

Fig. 37 As in Fig. 32 but for longwave heating. Contour intervals are 1 K/day (upper panel) and 0.03 K/day (lower panel).

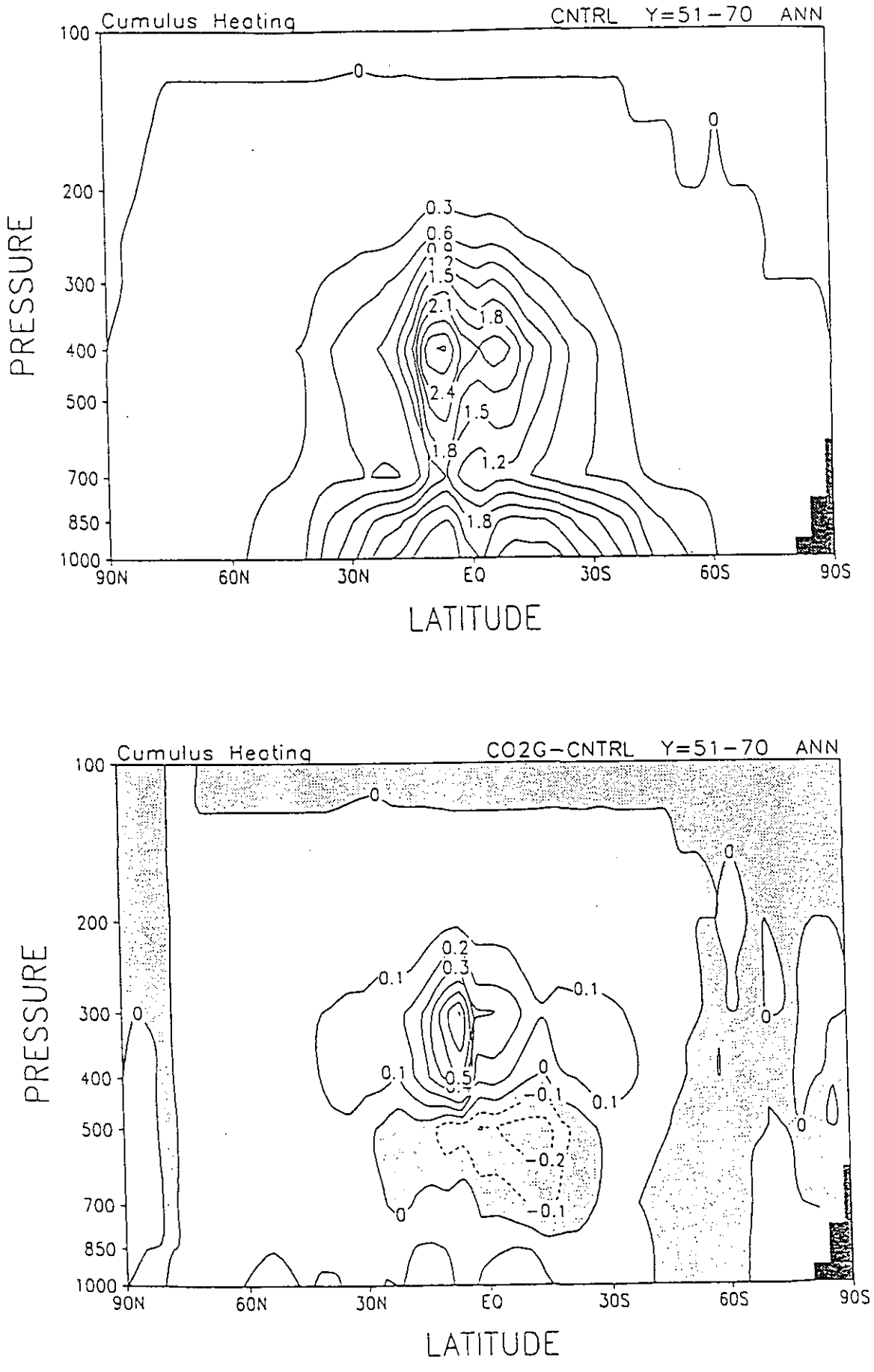

Fig. 38 As in Fig. 32 but for cumulus heating. Contour intervals are 0.3 K/day (upper panel) and 0.1 K/day (lower panel).

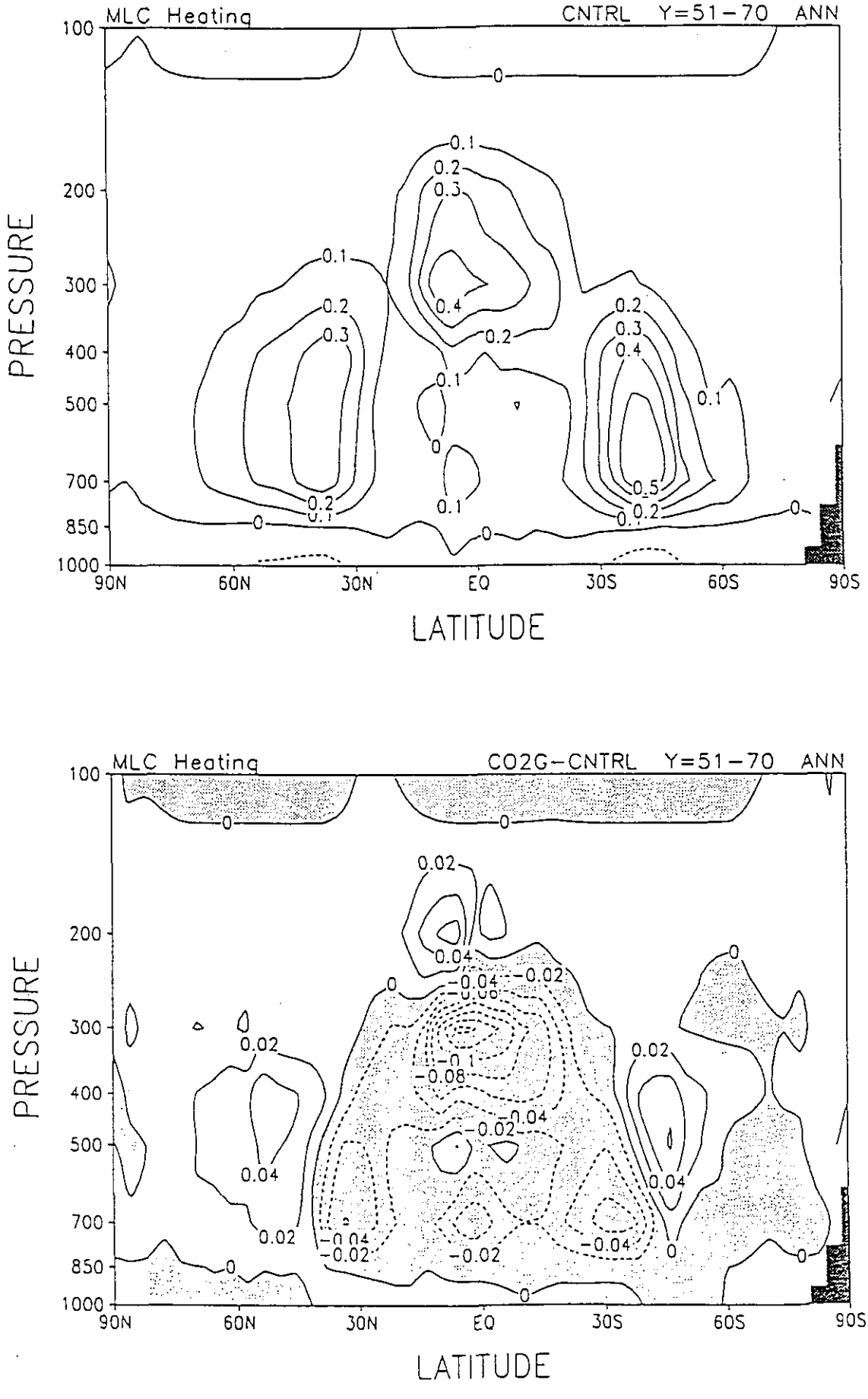

Fig. 39 As in Fig. 32 but for middle level convection heating. Contour intervals are 0.1 K/day (upper panel) and 0.02 K/day (lower panel).

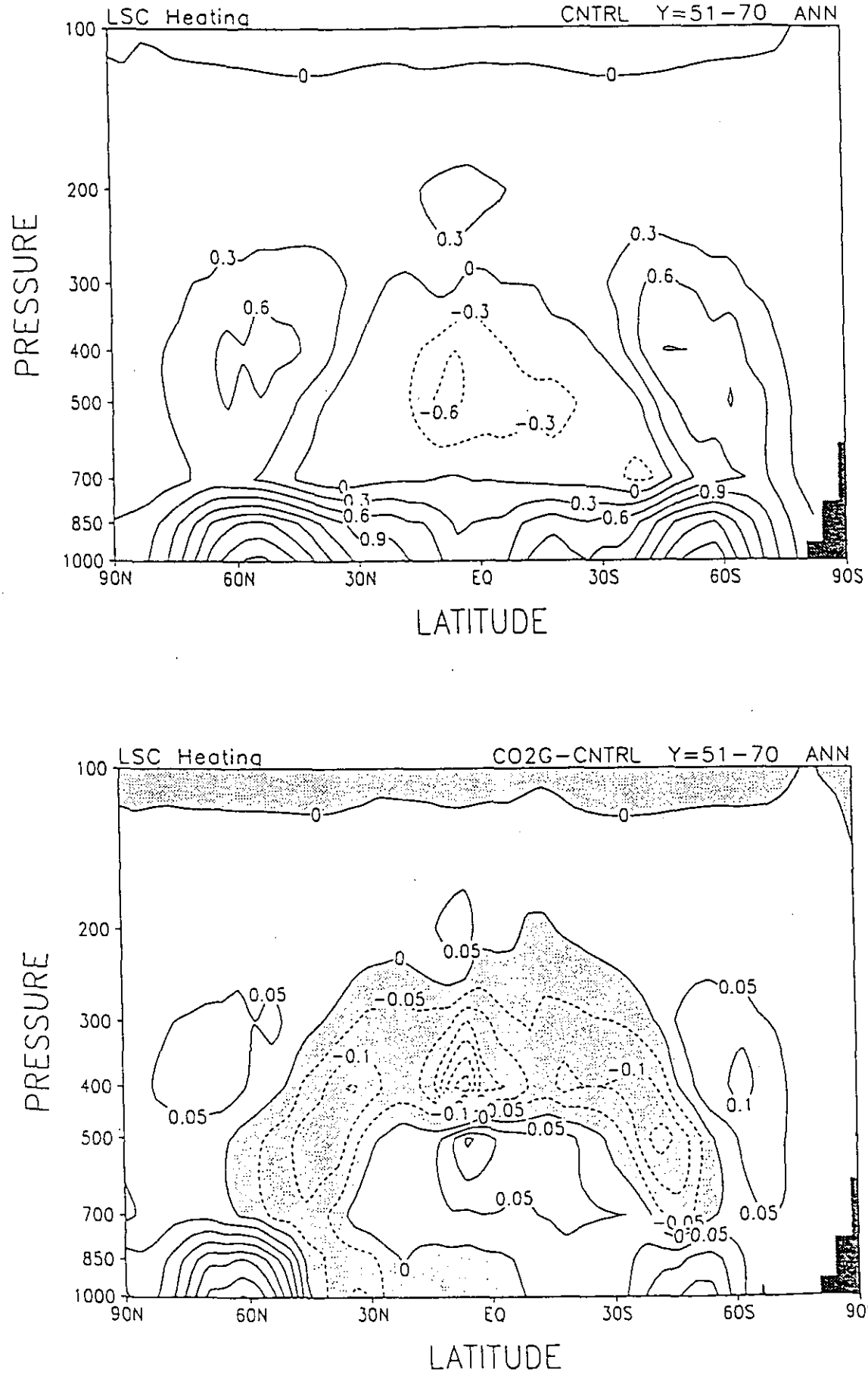

Fig. 40 As in Fig. 32 but for large scale condensation heating. Contour intervals are 0.3 K/day (upper panel) and 0.05 K/day (lower panel).

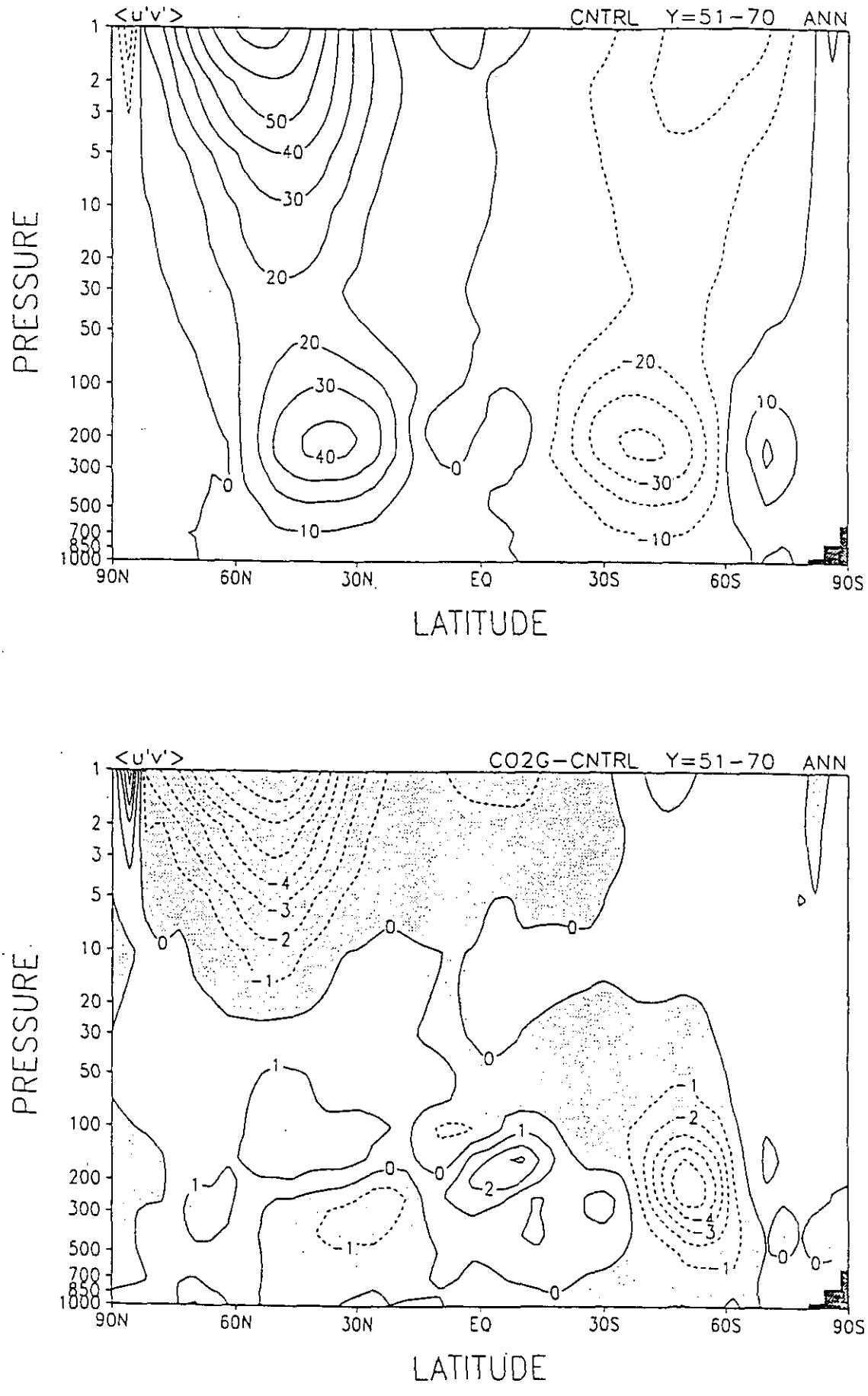

Fig. 41 As in Fig. 32 but for meridional eddy momentum transport. Contour intervals are 10 m^2/s^2 (upper panel) and 1 m^2/s^2 (lower panel).

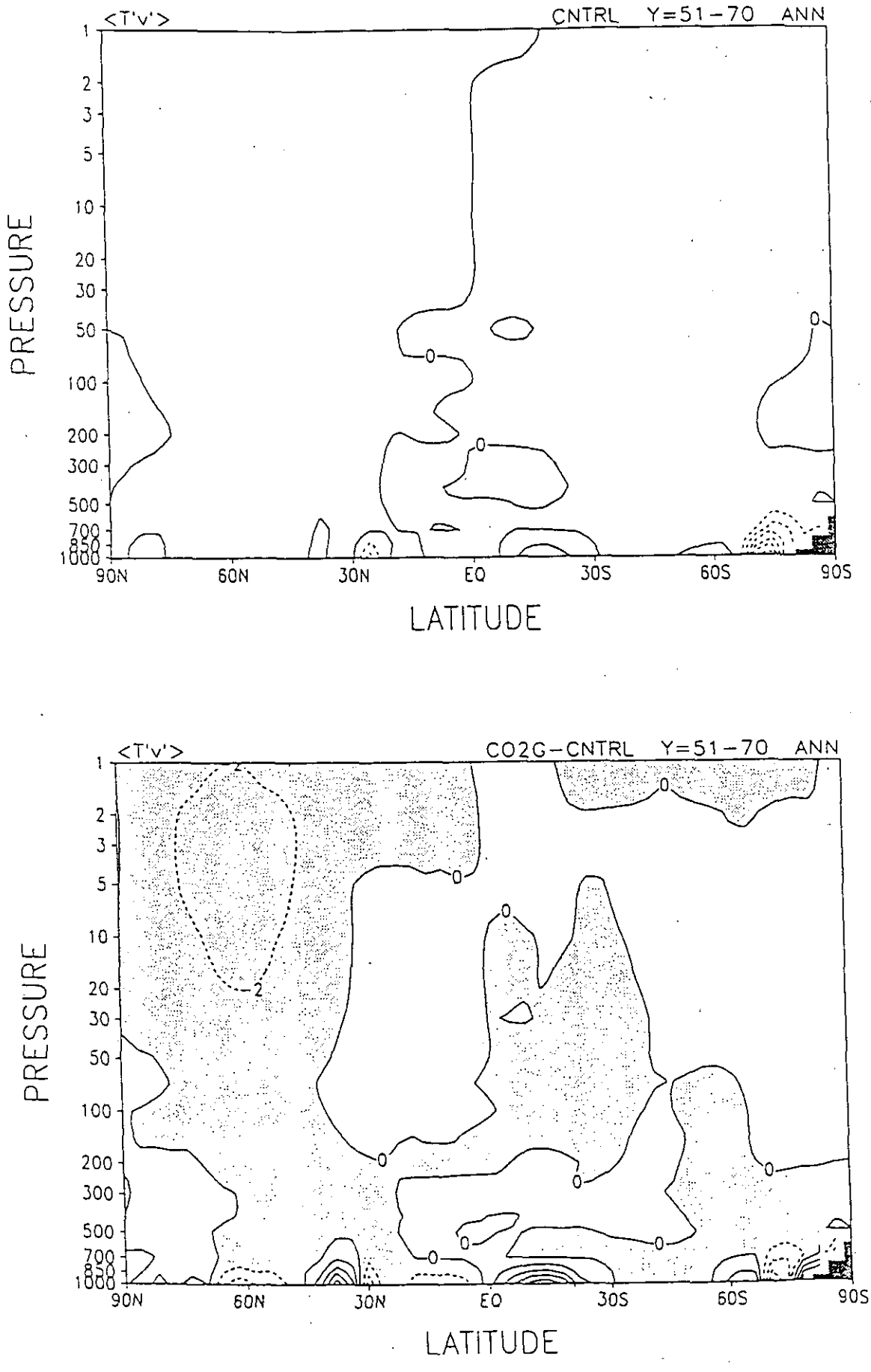

Fig. 42 As in Fig. 32 but for meridional eddy heat transport. Contour intervals are 10 Km/s (upper panel) and 2 Km/s (lower panel).